Title

Does crystallographic anisotropy prevent the conventional treatment of aqueous mineral reactivity? A case study based on K-feldspar dissolution kinetics

Authors

Pollet-Villard, Marion

Daval, Damien

Ackerer, Philippe

et al.

Publication Date

2016-10-01

DOI

10.1016/j.gca.2016.07.007

Available online at www.sciencedirect.com

ScienceDirect

Geochimica et Cosmochimica Acta 190 (2016) 294–308

Geochimica et Cosmochimica Acta

www.elsevier.com/locate/gca

Does crystallographic anisotropy prevent the conventional treatment of aqueous mineral reactivity? A case study based on K-feldspar dissolution kinetics

Marion Pollet-Villard [a,*], Damien Daval [a,b], Philippe Ackerer [a], Giuseppe D. Saldi [b], Bastien Wild [a], Kevin G. Knauss [b], Bertrand Fritz [a]

[a] Laboratoire d'Hydrologie et de Géochimie de Strasbourg, Université de Strasbourg/EOST, CNRS, 67084 Strasbourg, France
[b] Earth Sciences Division, Lawrence Berkeley National Laboratory, Berkeley, CA 94720, USA

Received 3 March 2016; accepted in revised form 7 July 2016; Available online 15 July 2016

Abstract

Which conceptual framework should be preferred to develop mineral dissolution rate laws, and how the aqueous mineral reactivity should be measured? For over 30 years, the classical strategy to model solid dissolution over large space and time scales has relied on so-called kinetic rate laws derived from powder dissolution experiments. In the present study, we provide detailed investigations of the dissolution kinetics of K-feldspar as a function of surface orientation and chemical affinity which question the commonplace belief that elementary mechanisms and resulting rate laws can be retrieved from conventional powder dissolution experiments. Nanometer-scale surface measurements evidenced that K-feldspar dissolution is an anisotropic process, where the face-specific dissolution rate satisfactorily agrees with the periodic bond chain (PBC) theory. The chemical affinity of the reaction was shown to impact differently the various faces of a single crystal, controlling the spontaneous nucleation of etch pits which, in turn, drive the dissolution process. These results were used to develop a simple numerical model which revealed that single crystal dissolution rates vary with reaction progress. Overall, these results cast doubt on the conventional protocol which is used to measure mineral dissolution rates and develop kinetic rate laws, because mineral reactivity is intimately related to the morphology of dissolving crystals, which remains totally uncontrolled in powder dissolution experiments. Beyond offering an interpretive framework to understand the large discrepancies consistently reported between sources and across space scales, the recognition of the anisotropy of crystal reactivity challenges the classical approach for modeling dissolution and weathering, and may be drawn upon to develop alternative treatments of aqueous mineral reactivity.

Keywords: Orthoclase; Dissolution; Kinetic rate laws; Gibbs free energy; Crystallographic orientation; Dissolution anisotropy

1. INTRODUCTION

Chemical weathering spontaneously affects most solids including building and industrial materials (e.g. Nicoleau et al., 2013; King et al., 2014; Hellmann et al., 2015), biomaterials (e.g. Derry et al., 2005) or geomaterials (e.g. Lasaga and Lüttge, 2001). Accordingly, mineral dissolution drives a series of fundamental processes of industrial (e.g. CO_2 sequestration (Knauss et al., 2005; Saldi et al., 2015), enhanced geothermal systems (Fritz et al., 2010)), biological (e.g. nutrient supply, see Lower et al., 2001) and geologic (e.g. carbon cycle Maher and Chamberlain, 2014) relevance. For most of these fields and in particular, in Earth

* Corresponding author.
E-mail address: polletvillard@unistra.fr (M. Pollet-Villard).

http://dx.doi.org/10.1016/j.gca.2016.07.007
0016-7037/

sciences, two main approaches have been commonly applied to model the fate of chemical weathering at large space and time scales. The first category of models relies on a phenomenological, top-down strategy where empirical relations between mineral dissolution and effective external forcing parameters such as temperature or runoff are used (Berner, 1990). Since the early 90s, this approach has been gradually superseded by reactive transport models, where mineral reactivity is accounted for via kinetic rate laws derived from dissolution experiments carried out on powdered single-crystals. This strategy now fuels most simulations of fluid-mineral interactions (see e.g. Knauss et al., 2005; Fritz et al., 2010; Beaulieu et al., 2012; Maher and Chamberlain, 2014).

Compared to the top-down approach, the bottom-up strategy is often praised for its presumably greater reliability. Because experiments are conducted on powdered materials under well-defined conditions, it is often claimed that the resulting kinetic rate laws supposedly reflect the underlying elementary dissolution and precipitation mechanisms (Schott et al., 2009), rendering the corresponding fluid-mineral simulations more robust.

In addition to their technical simplicity, measurements of bulk dissolution rates became widespread and conventional because of the conceptual framework in which the corresponding kinetic rate laws have been developed. Application of the transition state theory (TST) initially developed for elementary reactions in homogeneous media to overall dissolution processes in heterogeneous media was proposed in the early 80s (Aagaard and Helgeson, 1982), and subsequently coupled to surface complexation models (SCM), paving the way to the SCM/TST framework (Schott et al., 2009). A fundamental and appealing implication of applying this conceptual framework is that the complexity of heterogeneous chemical reactions is boiled down to the isotropic dissolution of a given solid, justifying the conventional measurement of bulk dissolution rates, and pushing to the background any potential crystallographic control on the reaction rate and rate law.

Arguably, the SCM/TST framework has succeeded in describing the dissolution of materials with simple chemistry and fairly high symmetry space-groups, such as simple metal oxides or hydroxides (e.g. Schott et al., 2009; Ohlin et al., 2010 and references therein). However, the detailed mechanisms and corresponding dissolution rate laws for more complex materials such as silicates are still a source of lively debate (e.g. Burch et al., 1993; Oelkers et al., 1994; Gautier et al., 1994; Lasaga and Lüttge, 2001; Hellmann and Tisserand, 2006; Beig and Lüttge, 2006; Hellmann et al., 2010; Gruber et al., 2014). More broadly, rate data collected via the conventional approach have long been shown to diverge from their field counterparts (White and Brantley, 2003), revealing inconsistencies of orders of magnitude for most minerals, even at the laboratory scale (Fischer et al., 2014), which questions the reliability of rate models developed on such datasets. As a matter of fact, aside from a limited number of studies which managed to reconcile experimental and field data at specific sites (e.g. Maher et al., 2009), upscaling laboratory results to the field without adjustments of several modeling parameters has essentially remained an elusive goal.

The source for the above-mentioned discrepancies remains an open question: aside from identified complicating factors including aqueous transport-limitations (Ruiz-Agudo et al., 2012; Laanait et al., 2015) or passivation by surface layers (Daval et al., 2011, 2013), a handful of recent studies has pointed out that mineral surfaces do not homogeneously and isotropically react with aqueous fluids (Godinho et al., 2012, 2014; Daval et al., 2013; Fischer et al., 2014; Laanait et al., 2015). Although crystallographic control of aqueous mineral reactivity has been suggested for decades (e.g. Gratz et al., 1991), the lack of quantitative data coupled to the potential problems inherent to the difficulties associated with modeling of anisotropic dissolution (such as tracking mineral texture over time in reactive transport codes), the heterogeneity and anisotropic nature of the dissolution process has long remained overlooked. In fact, the recognition that atomic ordering primarily impacts solid reactivity is relatively new, essentially resulting from the advent of microscopic, spectroscopic and computational methods allowing one to probe heterogeneous reactions at the molecular-level (e.g. Yanina and Rosso, 2008; Bandstra and Brantley, 2008; Kubicki et al., 2012; Daval et al., 2013; Lüttge et al., 2013; Kurganskaya and Lüttge, 2013; Fenter et al., 2014). Taken together, these recent observations motivated the present study, aimed at clarifying the validity and limitations of the conventional protocol commonly used to measure and upscale mineral dissolution rates.

Below, we provide measurements of K-feldspar (orthoclase, $KAlSi_3O_8$) dissolution, considered as a model mineral. Orthoclase was selected because of (1) its chemical composition and low-symmetry space-group, which substantially deviate from simple oxides/hydroxides for which the SCM/TST model putatively applies, (2) the fairly large dataset related to the bulk dissolution kinetics and dissolving surface structure of orthoclase (see Gautier et al., 1994; Fenter et al., 2014 and references therein) and feldspars as a whole (Beig and Lüttge, 2006; Hellmann and Tisserand, 2006; Hellmann et al., 2010) and (3) undoubtedly, the relevance of feldspar dissolution for major processes such as atmospheric CO_2 drawdown through continental weathering of silicates (Kampman et al., 2009). As opposed to previously applied methods (e.g. Gautier et al., 1994; Hellmann and Tisserand, 2006) and following the pioneering measurements of Lüttge et al. (1999), our study benefited from the use of vertical scanning interferometry (VSI) technique to monitor orthoclase dissolution kinetics as a function of surface orientation and chemical affinity, which represents the driving force for any chemical reaction and is consequently the most fundamental parameter to be investigated.

2. MATERIALS AND METHODS

2.1. Sample characterization and preparation

The starting material is a natural orthoclase single crystal from Afghanistan. No minor phases were detected with

X-ray diffraction or scanning electron microscopy (SEM). Monolithic orthoclase samples (tens to several mm on a side) were cut with a diamond blade saw and polished through a multi-step abrasive sequence using diamond suspensions of decreasing grain sizes and soft polishing cloths, with an ultimate polishing step in a colloidal silica suspension. Although such treatments were previously shown to potentially increase the density of shallow (<100 nm-deep) damage, they were also shown to negligibly affect the defect density of the inner mineral volume (e.g. Lucca et al., 2006). The crystallographic orientation of each sample was determined using an electron backscatter diffraction (EBSD) detector attached to the SEM (TESCAN® Vega 2). The initial roughness of each surface was measured at different scales with vertical scanning interferometer (ZYGO® NewView 7300). For each sample, the initial average arithmetic roughness (*Ra*), defined as the arithmetic average of the absolute values of the roughness profile, ranged between 5 nm and 20 nm, and *Rq* (the roughness calculated with the root-mean-square of the vertical distance between the surface elevation and the mean surface line) ranged between 7 nm and 28 nm. These initial roughness parameters were measured on 270 × 360 μm^2 VSI images.

2.2. Aqueous dissolution experiments

Oriented samples were mounted in a titanium support as designed by Daval et al. (2013) (Fig. 1a), where a Viton® disk held with a screw creates a non-wetted reference area. Partially masked samples were reacted in a synthetic alkaline solution in Parr® mixed-flow reactor at 180 °C and 50 bars for durations ranging from one to three weeks to check for the linearity of the surface retreat as a function of time. In this set-up, the pressure is kept constant through the use of a back pressure regulator (Grove Mity Mite® S91XW), and the aqueous solution was continuously stirred thanks to a magnetic stirrer rotating at a constant speed of 125 RPM. Such rotation speeds are usually sufficient to ensure dissolution rates that are not transport-controlled for the range of mineral reactivity which is considered (see e.g. Saldi et al., 2013). Inlet solutions were made with ultrapure deionized water (18.2 MΩ cm^{-1}) and analytical grade NaOH, KCl, $AlCl_3$ and Na_2SiO_3. The pH was adjusted with the concentration of NaOH in the solution ($pH_{in\ situ\text{-}180°C} = 9.1 \pm 0.3$). No pH buffer was used in solution because, as it has been generally observed, buffers can influence the dissolution rate of silicates (e.g. Golubev and Pokrovsky, 2006). Investigating the dissolution of K-feldspar in alkaline solutions ensures that the dissolution process is not influenced by the formation of amorphous silica-rich surface layers (Hellmann et al., 1997) which could ultimately control the dissolution rate of the silicate mineral (e.g. Daval et al., 2013; Maher et al., 2016). The Al concentration was kept constant ([Al] = 3.8 ± 0.5 ppm) for each experiment to get rid of any potential inhibitory effect that Al may play on the dissolution rate, as suggested in several studies (Gautier et al., 1994). The concentration of the others chemical species was varied to investigate different values of the Gibbs free energy of orthoclase dissolution (Δ*G*). During experiments, the outlet fluid was sampled every day. Compositions of the inlet and the outlet solutions were measured by ICP-AES (THERMO ICAP 6000 Series). Aqueous concentrations at steady-state conditions are listed in Table 1. The CHESS code (van der Lee and De Windt, 2002) was used to determine the *in situ* pH and saturation indices with respect to orthoclase and secondary phases. It was verified that all solutions were undersaturated with respect to any secondary phase.

2.3. Vertical scanning interferometry (VSI) surface topography measurements

After dissolution experiments, sample surfaces were analyzed with VSI in stitching mode (magnification: ×5) to estimate the average change in height between the unreacted reference surface and the reacted mineral surface

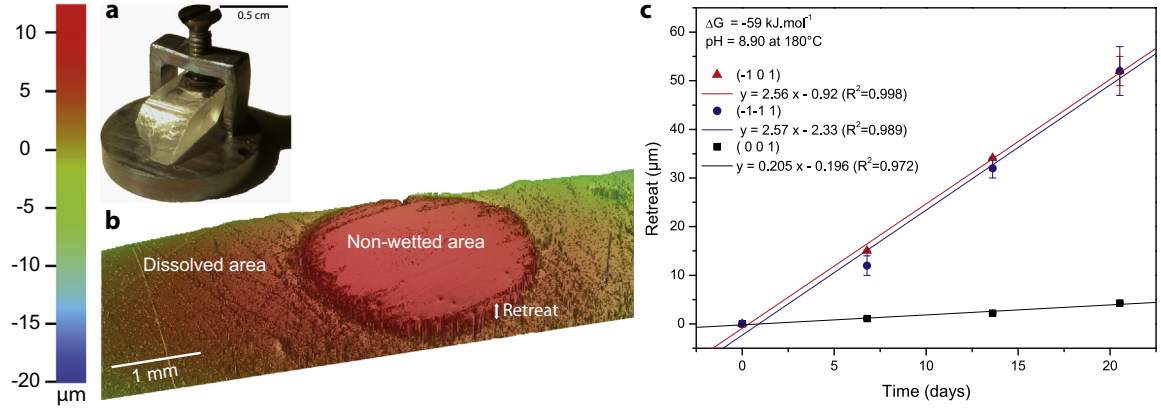

Fig. 1. Surface retreat measurements after face-specific dissolution experiments. (a) After initial surface roughness measurements by AFM and VSI, K-feldspar sample was mounted on a passivated titanium jig. A Viton disk held with a screw creates a non-wetted reference surface. The crystal is subsequently altered in a flow-through reactor at 180 °C in a synthetic alkaline solution. (b) Illustrative 3D-view of face $(\bar{1}\,\bar{1}\,1)$ realized by VSI after one week of alteration, evidencing a typical surface retreat between the non-wetted reference area and the dissolved area. (c) Surface retreat measurements carried out on faces $(\bar{1}\,0\,1)$, $(\bar{1}\,\bar{1}\,1)$ and (0 0 1) as a function of time (see Tables 1–3 for details regarding the corresponding MRGT2 experiment). The surface retreat is linear with time (i.e., the dissolution rate is constant) but depends on the crystallographic orientation: a tenfold factor is observed between the slowest face (0 0 1) and the others.

Table 1
Summary of experimental and calculated aqueous data of face-specific K-feldspar dissolution experiments. Columns 1–4 indicate: the name of experiment, the total time duration of experiment (days), the flow-rate v of the pump (mL min^{-1}) and the $pH_{in\ situ}$ calculated with the CHESS code. The *in situ* solution compositions (in ppm) are listed in the five next columns. Fluid concentration measurements, excepted for [Cl], were carried out with ICP-AES. The two last columns present the ionic strength (mol L^{-1}) of the solution and the ΔG (kJ mol^{-1}) value with respect to K-feldspar dissolution calculated using CHESS.

Expt.	t (days)	v (mL min^{-1})	$pH_{in\ situ\ 180°C}$	Concentrations out (ppm)					Ionic strength (mol L^{-1})	ΔG (kJ mol^{-1})
				[Si]	[Al]	[K]	[Na]	[Cl]		
MRG1	6.8	0.07	8.9	3.20	4.29	1.18	92.54	22.61	4.04E−03	−49
MRG2	7.0	0.07	8.9	3.23	4.32	1.46	92.34	13.77	4.04E−03	−48
MRG3	6.9	0.10	9.5	87.63	3.53	43.40	252.89	52.73	1.18E−02	−6
MRG4	7.0	0.10	9.5	85.66	3.29	42.62	252.89	52.08	1.18E−02	−7
MRG5	6.9	0.10	9.0	8.23	4.10	3.52	114.99	17.16	5.06E−03	−36
MRG6	7.0	0.10	9.0	8.51	4.26	3.72	115.04	17.10	5.07E−03	−35
MRG7	6.9	0.34	9.2	0.64	3.64	0.22	183.94	13.72	7.96E−03	−81
MRG8	6.9	0.35	9.2	0.65	3.61	0.20	183.94	13.46	7.96E−03	−81
MRG9	7.0	0.10	9.2	41.33	3.62	17.06	184.13	27.43	8.31E−03	−16
MRG10	6.8	0.10	9.2	43.66	3.63	22.74	184.18	31.97	8.46E−03	−14
MRG11	6.9	0.10	9.5	62.34	3.40	29.98	391.83	32.99	1.73E−02	−18
MRG12	6.9	0.10	9.5	64.07	3.67	28.69	390.83	41.14	1.73E−02	−17
MRG13	6.9	0.10	9.5	85.06	3.55	39.00	391.21	45.74	1.74E−02	−13
MRG14	7.0	0.10	9.5	86.41	3.69	37.27	390.83	48.09	1.74E−02	−12
MRG15	6.9	0.26	8.9	0.58	3.78	0.24	91.98	14.43	3.99E−03	−75
MRG16	6.9	0.26	8.9	0.78	3.81	0.30	91.99	14.36	4.00E−03	−71
MRG17	6.9	0.38	8.9	0.39	3.74	0.15	91.98	14.41	3.99E−03	−81
MRG18	6.8	0.38	9.2	0.91	3.81	0.38	160.97	14.00	6.97E−03	−77
MRG19	6.8	0.10	9.1	22.25	3.64	10.57	161.01	22.04	7.19E−03	−24
MRG20	6.8	0.10	9.1	23.10	4.05	10.21	160.97	22.75	7.18E−03	−23
MRGP1	6.9	0.23	9.2	3.03	3.55	1.24	161.06	9.04	7.00E−03	−55
MRGP2	7.7	0.24	9.3	4.24	3.58	1.62	195.58	0.00	8.49E−03	−53
MRGT1	4.8	0.20	9.0	0.25	3.99	0.12	114.96	12.82	4.99E−03	−89
MRGT2	20.5	0.20	8.9	1.45	3.78	1.11	97.09	13.58	4.23E−03	−59
MRGT3	3.5	0.20	8.9	2.19	3.71	1.32	101.29	13.83	4.43E−03	−54

(Fig. 1b). For each oriented sample, dissolution rates were calculated according to the following equation (see e.g. Arvidson et al., 2004):

$$r^{(hkl)} = \frac{\Delta h}{\Delta t}\bar{V}^{-1} \quad (1)$$

where $r^{(hkl)}$ (mol m^{-2} s^{-1}) is the dissolution rate of the (hkl) face, Δh is the surface retreat, Δt is the alteration duration and $\bar{V}$ (m^3 mol^{-1}) is the molar volume of orthoclase.

Surface imaging at higher magnification (×10 to ×100) was also achieved in order to quantify the etch pit density. The images were subsequently processed by color thresholding using the ImageJ software (Abramoff et al., 2004; Schneider et al., 2012). Measurements were performed after equal time durations on faces (0 0 1), (0 1 0), $(\bar{1}\,1\,0)$, $(1\,\bar{3}\,0)$ and $(\bar{1}\,\bar{1}\,1)$ over the entire range of ΔG conditions that was investigated. The statistical analysis of pits covering the $(\bar{1}\,0\,1)$ face was not possible because of the complex surface features of this face, possibly resulting from the extensive coalescence of etch pits which prevented the above-described image processing.

3. RESULTS

3.1. Face-specific dissolution rate of K-feldspar

The surface retreat measurements and associated dissolution rates of 6 natural faces of orthoclase were calculated and are listed in Tables 2 and 3, respectively. Because the application of Eq. (1) requires that the overall surface retreat is a linear function of time, the temporal evolution of the surface retreat was monitored on several selected experimental conditions for durations of up to 3 weeks (Fig. 1c and Table 2). These specific experiments verified that the surface retreat increases linearly with time.

The rate data are reported as a function of ΔG in Fig. 2. To get rid of any contribution to the measured dissolution rates of the slight variations in pH from one experiment to the other, the measured experimental K-feldspar dissolution rates (blue triangles) were corrected and recalculated for an exact pH of 9.0, based on the pH-dependence of K-feldspar dissolution given by Palandri and Kharaka (2004) (black squares) (see Daval et al., 2010 for previous similar treatment). Of note, this correction assumes that the pH-dependence is the same for all faces. To the best of our knowledge, whether or not the pH-dependence of K-feldspar dissolution varies with crystallographic orientation is unknown. However, for most cases, the pH variations were very modest, resulting in limited variations of the adjusted rate values. The solid black lines (Fig. 2) represent non-linear least-squares curve fittings (Levenberg–Marquardt method) using the phenomenological relation of Hellmann and Tisserand, 2006. The fitting parameters are listed in Table 4 – note that the actual values of the fitted parameters are not meant to be related to any specific molecular mechanism at that stage. In fact, our main

Table 2
Surface retreat measurements. The first two columns indicate the name of experiment and the time duration. The surface retreats measured by VSI in stitching mode with 5×-magnification are listed in the next three columns (μm). The left part of the table present results for (010), $(\bar{1}\,\bar{1}\,1)$ and $(1\,\bar{3}\,0)$ faces and on the right are results for (001), $(\bar{1}01)$, $(\bar{1}10)$ faces.

Expt.	t (days)	Surface retreat Δh (μm)			Expt.	t (days)	Surface retreat Δh (μm)		
		(010)	$(\bar{1}\,\bar{1}\,1)$	$(1\,\bar{3}\,0)$			(001)	$(\bar{1}01)$	$(\bar{1}10)$
MRG1	6.8	1.1 ± 0.3	5.1 ± 0.2	1.4 ± 0.1	MRG2	7.0	1.2 ± 0.2	12.0 ± 0.2	2.6 ± 0.2
MRG3	6.9	0.11 ± 0.02	0.4 ± 0.1	0	MRG4	7.0	0	0	0
MRG5	6.9	2.4 ± 0.7	7 ± 2	1.2 ± 0.3	MRG6	7.0	0.39 ± 0.05	10.1 ± 0.1	1.1 ± 0.3
MRG7	6.9	1.6 ± 0.7	18 ± 2	2.8 ± 0.5	MRG8	6.9	2.3 ± 0.7	17.4 ± 0.3	2.7 ± 0.7
MRG9	7.0	0.5 ± 0.2	2 ± 0.5	0.3 ± 0.1	MRG10	6.8	0.2 ± 0.1	3.6 ± 0.1	0.32 ± 0.02
MRG11	6.9	0.05 ± 0.03	0.8 ± 0.5	0.6 ± 0.3	MRG12	6.9	0.14 ± 0.05	2.3 ± 0.1	0.6 ± 0.3
MRG13	6.9	0.19 ± 0.04	0.4 ± 0.1	0.1 ± 0.05	MRG14	7.0	0.1 ± 0.05	0.76 ± 0.03	0.14 ± 0.05
MRG15	6.9	2.4 ± 0.5	10.8 ± 0.3	2.3 ± 0.4	MRG16	6.9	1.6 ± 0.2	10.85 ± 0.05	1.6 ± 0.3
MRG17	6.9	1.8 ± 0.5	9.3 ± 0.5	1.7 ± 0.3	MRG18	6.8	2.1 ± 0.2		2.7 ± 0.2
MRG19	6.8	0.5 ± 0.2	5.4 ± 0.1	1.4 ± 0.2	MRG20_01	6.8	0.28 ± 0.05	9.3 ± 0.3	
					MRG20_02	6.8	0.4 ± 0.2		
MRGT1					MRGT1				
t_1	1.6	0.13 ± 0.02			t_1	1.6	0.24 ± 0.05		
t_2	2.2	0.20 ± 0.05			t_2	2.2	0.32 ± 0.05		
t_3	4.8	0.7 ± 0.2			t_3	4.8	0.9 ± 0.1		
MRGT2					MRGT2				
t_1	6.8		12 ± 2		t_1	6.8	1.1 ± 0.1	15.0 ± 0.2	
t_2	13.6		32 ± 2		t_2	13.6	2.2 ± 0.1	34.1 ± 0.2	
t_3	20.5		52 ± 5		t_3	20.5	4.3 ± 0.1	52 ± 3	
MRGT3					MRGT3				
t_1	1.79	1.8 ± 0.5	4.2 ± 0.5	1.0 ± 0.2	t_1	1.79	0.5 ± 0.2		
t_2	3.5	2.5 ± 0.5	8.0 ± 0.5	1.5 ± 0.5	t_2	3.5	1.0 ± 0.2		

concern was to propose an *ad hoc* curve which could adequately fit our experimental datasets to ultimately provide overall r–ΔG relations for the arbitrary crystal morphologies reported in Fig. 4. Solid red lines are rate-curves based on the transition state theory.

The relation between $r^{(hkl)}$ and ΔG is apparently specific to the crystallographic orientation which is considered, since the dissolution rate plateau value observed at far-from-equilibrium conditions is different for each face (Fig. 2). The face-specific dissolution rates $r^{(hkl)}$ observe the following trend: $r^{(001)} \approx r^{(010)} \approx r^{(\bar{1}10)} \lesssim r^{(1\bar{3}0)} \ll r^{(\bar{1}01)} \approx r^{(\bar{1}\bar{1}1)}$. A tenfold factor is measured between the rate plateau value of the slowest dissolving face (001) and the fastest dissolving face $(\bar{1}\,\bar{1}\,1)$. In addition, the shape of the r–ΔG relations also depends on the crystallographic orientation. Whereas the (001), (010) and $(\bar{1}10)$ faces exhibit a relatively well-defined switch from rapid to slower dissolution rate, the dissolution rate of the $(\bar{1}01)$, $(\bar{1}\,\bar{1}\,1)$ and $(1\,\bar{3}\,0)$ faces decreases more gradually as ΔG increases. Finally, one can notice that the r–ΔG relations are systematically at odds with the TST-based relation implemented in most reactive transport codes.

3.2. Face-specific microstructural aspects of K-feldspar surfaces

The time-resolved growth and coalescence of etch pits was monitored on selected experiments, and when possible, the etch pit density was systematically measured after equal time durations for all experiments. These measurements evidenced that the anisotropic reactivity of K-feldspar is also reflected in the microstructural features of the different surfaces (Fig. 3). Regarding the (001), (010) and $(\bar{1}10)$ faces, abundant μm-deep 3D etch pits can be observed at far-from-equilibrium conditions. For $-45 < \Delta G < -20$ kJ mol^{-1}, the etch pit surface density dramatically drops, and much scarcer 2-D flat bottom pits likely originating from point defects is observed. On the other hand, for $(\bar{1}\,\bar{1}\,1)$ and $(1\,\bar{3}\,0)$ faces, the 3D etch pits surface density remains relatively constant over the entire range of Gibbs free energies that was considered.

Overall, these results suggest that the dissolution rate of K-feldspar is tightly related to its surface microstructure, which critically depends on the crystallographic structure of K-feldspar. In the next section, we further expand the rationale which could justify such an assumption, and provide a critical analysis of the consequences of these findings.

4. DISCUSSION

4.1. Far-from-equilibrium dissolution rate as a function of surface orientation

Consistent with previous work (e.g. Zhang and Lüttge, 2009), the (010) and (001) surfaces are part of the less reactive faces of K-feldspar. As opposed to other classes of silicate minerals such as inosilicates (Daval et al., 2013) or phyllosilicates (Turpault and Trotignon, 1994) for which the anisotropic reactivity could be easily inferred from the connectedness of Si tetrahedrons in the crystallographic structure of the minerals, explaining the anisotropic reactivity of K-feldspar is more complex because feldspars belong the category of tectosilicates, which have a

Table 3
Calculated dissolution rates based on surface retreat measurements. The first two columns provide the name of experiment and the Gibbs free energy of the reaction with respect to K-feldspar dissolution. The next four columns indicate the $pH_{in\ situ}$ of the experiment and the dissolution rate of the different crystallographic orientations (in mol m^{-2} s^{-1}). The dissolution rates recalculated for an exact pH of 9.0, adjusted from measured r and based on the pH-dependence of K-feldspar dissolution given by Palandri and Kharaka (2004) are listed in the last three columns.

Expt.	ΔG (kJ mol^{-1})	pH	r ($\times 10^{-9}$ mol m^{-2} s^{-1})			r ($\times 10^{-9}$ mol m^{-2} s^{-1}) pH 9		
			(010)	$(\bar{1}\bar{1}1)$	$(1\bar{3}0)$	(010)	$(\bar{1}\bar{1}1)$	$(1\bar{3}0)$
MRG1	−49	8.9	18	82	23	21	100	27
MRG3	−6	9.5	1.7	6.3	0	0.7	2.5	0
MRG5	−36	9.0	38	111	19	39	113	19
MRG7	−81	9.2	25	284	44	17	186	29
MRG9	−16	9.2	7.8	31	4.7	5,8	23	3,5
MRG11	−18	9.5	0.8	13	9.5	0.3	4.9	3.7
MRG13	−13	9.5	3.0	6.4	1.6	1.2	2.6	0.6
MRG15	−75	8.9	38	172	37	46	208	44
MRG17	−81	8.9	29	148	27	35	179	33
MRG19	−24	9.1	8.0	86	22	6.3	68	18
MRGT1	−89	9.0	15			15		
MRGT2	−59	8.9		271			310	
MRGT3	−54	8.9	83	258	50	100	312	60
Expt.	ΔG (kJ mol^{-1})	pH	r ($\times 10^{-9}$ mol m^{-2} s^{-1})			r ($\times 10^{-9}$ mol m^{-2} s^{-1}) pH 9		
			(001)	$(\bar{1}01)$	$(\bar{1}10)$	(001)	$(\bar{1}01)$	$(\bar{1}10)$
MRG2	−48	8.9	19	188	41	23	228	49
MRG4	−7	9.5	0	0	0	0	0	0
MRG6	−35	9.0	6.1	157	17	6.2	160	17
MRG8	−81	9.2	37	277	43	24	181	28
MRG10	−14	9.2	3.2	58	5.1	2.4	43	3.8
MRG12	−17	9.5	2.2	36	9.5	0.9	14	3.7
MRG14	−12	9.5	1.6	12	2.2	0.6	4.9	0.9
MRG16	−71	8.9	25	172	25	31	208	31
MRG18	−77	9.2	34		43	25		32
MRG20_01	−23	9.1	4.5	149		3.6	118	
MRG20_02	−23	9.1	6.4			5.1		
MRGT1	−89	9.0	19			18		
MRGT2	−59	8.9	21	280		24	320	
MRGT3	−54	8.9	31			37		

three-dimensional framework of Si tetrahedra. As such, a suitable strategy consists in analyzing the data in the framework of the periodic bond chain (PBC) theory (Hartman and Perdok, 1955). The PBC theory states that crystal faces can be sorted out according to the number of uninterrupted chains of energetically strong bonds (PBC) they contain. Faces containing respectively $\geqslant 2$, 1 and no PBC are commonly termed F- (for flat), S- (for stepped) and K- (for kinked) faces. The structure of K-feldspar was studied by Woensdregt (1982) according to the PBC theory, who suggested to further subdivide the F category between F1 and F2 subcategories, which either contain only the strongest PBCs of the structure (with only Al–O or Si–O bonds) (F1), or also contain weaker K–O PBC (F2). Interestingly, Woensdregt, 1982 proposed that faces $(\bar{1}10)$, (001) and (010) belong to the F1 subcategory, as opposed to faces $(\bar{1}01)$, $(\bar{1}\bar{1}1)$ and $(1\bar{3}0)$, which belong to the F2 category. Therefore, with the exception of face $(1\bar{3}0)$ (cf. Section 3.1; see also Section 4.2 for further discussion), our measurements verify that face reactivity is correlated with the strength of the bonds they contain, as expected from the PBC theory.

4.2. Face-specific dissolution rates as a function of ΔG

The anisotropic nature of the dissolution process is further confirmed when the whole range of chemical affinities is considered (Fig. 2). According to our results, F1 faces exhibit a relatively well-defined switch from rapid to slower dissolution rate, whereas dissolution rate decreases more gradually as ΔG increases in the case of F2 faces (Figs. 2 and 4).

The divergence between the reactivity of F1 and F2 faces is also reflected by the microstructural aspects of the different surfaces (Fig. 3). As stated above, the etch pit density drastically decreases when approaching equilibrium for F1 faces; in contrast, F2 faces are characterized by a relatively constant density of μm-deep 3D etch pits typically originating from outcropping dislocations (e.g. Gratz et al., 1991), regardless of ΔG.

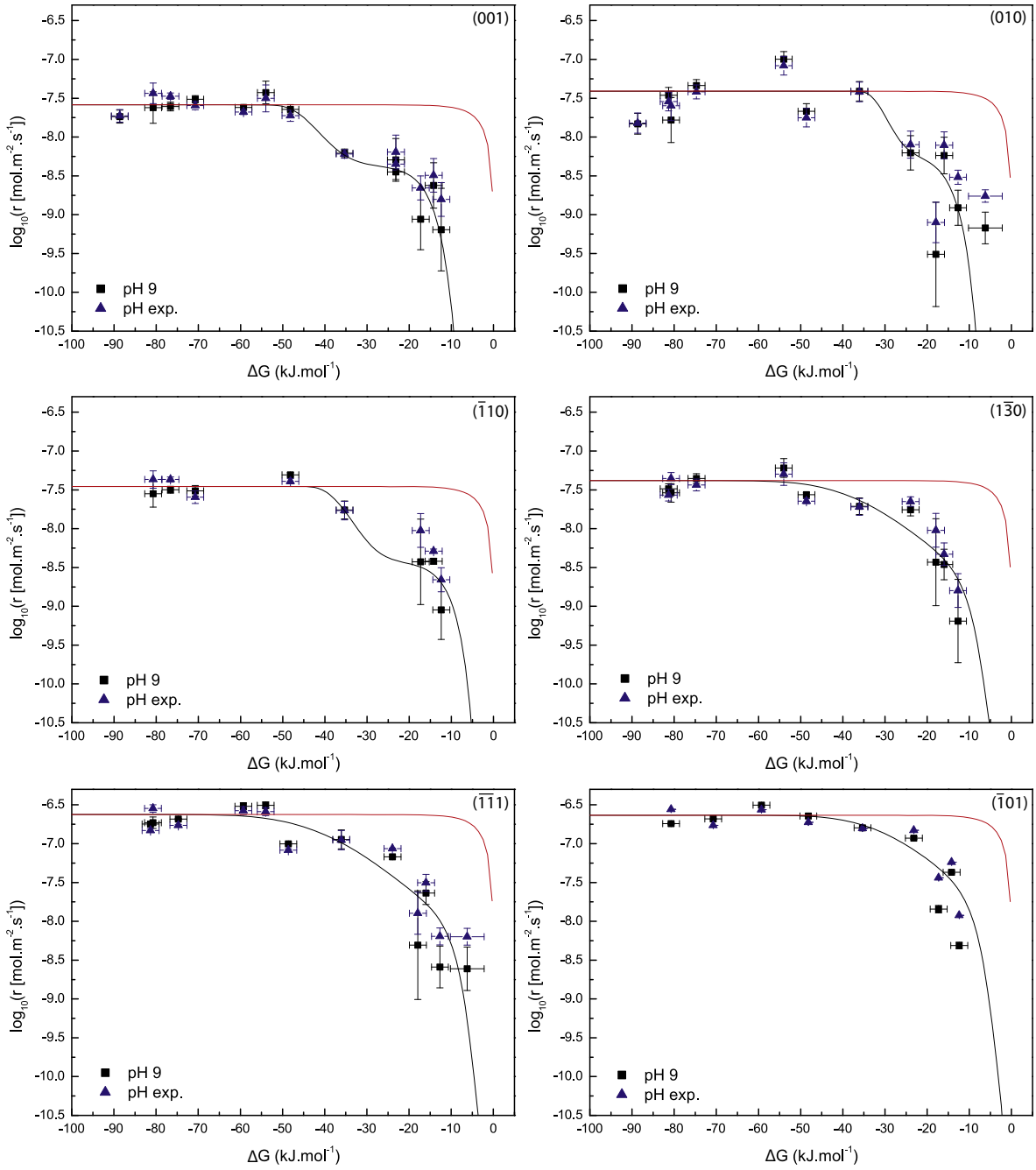

Fig. 2. r–ΔG relations for the six crystallographic orientations investigated in the present study: (001), (010), ($\bar{1}$10), (1$\bar{3}$0), ($\bar{1}\bar{1}$1) and ($\bar{1}$01). Dissolution experiments were carried out at 180 °C and $pH_{in\ situ} = 9.1 \pm 0.3$. To remove any contribution of the slight variations in pH from one experiment to the other, the measured experimental K-feldspar dissolution rates (blue triangles) were corrected and recalculated for an exact pH of 9.0, based on the pH dependence of K-feldspar given by Palandri and Kharaka (2004) (black squares). As can be seen, for most cases, such a treatment results in very modest variations of the adjusted rate values. The solid black lines represent non-linear least-squares curve fittings (Levenberg–Marquardt method) using the phenomenological relation of Hellmann and Tisserand (2006). The fitting parameters are listed in Table 4 – note that the actual values of the fitted parameters are not meant to be related to any specific molecular mechanism. In fact, our main concern was to propose an *ad hoc* curve which could adequately fit our experimental datasets to ultimately provide overall r–ΔG relations for the arbitrary crystal morphologies reported in Fig. 4. Solid red lines are rate-curves based on the transition state theory, for which the rate plateau has been adjusted to the mean far-from-equilibrium dissolution rate of the considered face. (For interpretation of the references to colour in this figure legend, the reader is referred to the web version of this article.)

These observations can be interpreted in the framework of the stepwave model (Lasaga and Lüttge, 2001), which states that etch pit nucleation is a major driver of crystal dissolution. Following this model, a critical free energy (ΔG^{crit}) value is required to open up etch pit at line defects spontaneously, the pit walls representing a continuous

Table 4
Fitting parameters of r–ΔG relations based on an overall rate law adapted from Hellmann and Tisserand (2006): $r = k_0[\alpha(1-\exp(-ng^{m_1}))+(1-\alpha)(1-\exp(-g))^{m_2}]$, where k_0 is the rate plateau in mol m^{-2} s^{-1}, α is a dimensionless number that has been determined by regression, $g = |\Delta G|/RT$ and n, m_1 and m_2 are adjustable fitted parameters found with a non linear least-squares curve fitting (Levenberg–Marquardt method).

Face	k_0	α	n	m_1	m_2
(0 0 1)	2.60E−08	0.8350	3.96E−12	10.57	57.47
(0 1 0)	3.90E−08	0.8454	2.96E−12	12.45	46.70
($\bar{1}$ 1 0)	3.50E−08	0.8920	9.82E−11	10.03	16.71
(1 $\bar{3}$ 0)	4.16E−08	0.9138	2.15E−04	3.59	23.11
($\bar{1}$ $\bar{1}$ 1)	2.37E−07	0.9410	1.52E−04	3.59	17.49
($\bar{1}$ 0 1)	2.32E−07	0.8743	8.72E−04	3.24	15.16

source of steps which travel throughout the crystal surface, eventually leading to its overall retreat. Conversely, if this energetic threshold is exceeded, etch pit nucleation at dislocation outcrops is no longer spontaneous, and the dissolution is essentially driven by point defects and dissolution on pre-existing corners and edges at a much slower rate.

Lasaga and Blum (1986) showed that a basic expression for calculating the numerical value of ΔG^{crit} at screw dislocations can be written as follows:

$$\Delta G^{crit} = \frac{-2\pi^2\sigma^2\bar{V}}{\mu b^2} \quad (2)$$

where σ is the surface free energy, $\bar{V}$ is the molar volume, μ is the bulk shear modulus, and b is the Burgers vector of the dislocation. As anticipated by Lasaga and Blum (1986) and confirmed in our study, this expression illustrates that several values of ΔG^{crit} may exist for a given mineral, depending on the surface energy of the specific face which is considered, and the length of the Burgers vectors outcropping at the crystal surface. Combining this expression with the classification of K-feldspar faces proposed by Woensdregt (1982) further indicate that the differences in ΔG^{crit} revealed in our study ($-45 < \Delta G < -20$ kJ mol^{-1} for F1 faces; $\Delta G > -10$ kJ mol^{-1} (if any) for F2 faces) may stem from the surface energy differences between F1 and F2 faces, since the PBC theory predicts that the surface energy of F1 faces deviates from that of F2 faces.

Overall, these results nicely illustrate that the differences in terms of microstructural features revealed at the μm-scale, which are directly inherited from the anisotropic distribution of atomic positions in the K-feldspar unit cell at the Å-scale, can have a major impact at the macro-scale and result in specific kinetic hallmarks, such as the observed discrepancies between the $r^{(F1)}$–ΔG and $r^{(F2)}$–ΔG trends. Consistent with our results, supposing that K-feldspar dissolution can be interpreted in the combined framework of the PBC and stepwave models leads to the following additional comments:

(i) The proposed intimate link between the macroscopic r–ΔG relations and corresponding microstructural aspects of the dissolving surface is in close agreement with recent published work. For instance, Arvidson and Lüttge (2010) demonstrated that a steep kinetic drop is observed for albite crystal surfaces (0 0 1) when the starting etch pit density is dramatically decreased. Conversely, r–ΔG relations such as those observed for F2 faces where the decrease of the dissolution rate is a gradual function of the chemical affinity is typical of pit-dominated dissolution regardless of the free energy which is considered, as previously shown by Beig and Lüttge (2006).

(ii) It may seem intriguing that the surface retreat is a linear function of time, in spite of the growing density of etch pits that nucleate on the various surfaces of K-feldspar. For instance, it has been recently proposed that the development of pit walls with lower surface energy was responsible for increasing the proportion of weakly reactive surface area, ultimately leading to an intrinsic decrease of the long-term dissolution rate of the considered surface (e.g. Godinho et al., 2012; Smith et al., 2013). As a matter of fact, this mechanism should have a great impact on the dissolution of surfaces with high initial reactive site densities, such as K- or S-faces, which were not investigated in the present study. If one states that K-feldspar reactivity complies with the PBC theory, then the pit walls developed on the F-faces cannot be less reactive than the F-faces themselves, which probably explain why the dissolution rate of the faces that were considered in the present study does not decline with time. Conversely, following simple geometric considerations, one could claim that the dissolution rate of a given surface should increase as a function of time, because of the additional surface area that is exposed to the solution due to the nucleation of etch pits. While this question will be addressed in detail in an upcoming companion study, as a preliminary piece of evidence, we roughly estimated the increase in surface area resulting from the development of pit walls on the (0 0 1) surface. Such an increase never exceeded 20% for all experiments, which is on the same order of magnitude as the spatial variability of the measured surface retreat (see Table 2), and any intrinsic temporal increase of the face-specific dissolution rate should be considered as speculative at that stage.

(iii) Finally, although our rate data are consistent with the PBC theory for 5 out of the 6 investigated crystallographic orientations, the use of the PBC theory cannot easily account for the anomalously slow reactivity of the (1 $\bar{3}$ 0) face. A tentative explanation may rely on the anisotropic distribution of dislocations in the K-feldspar structure: as described in

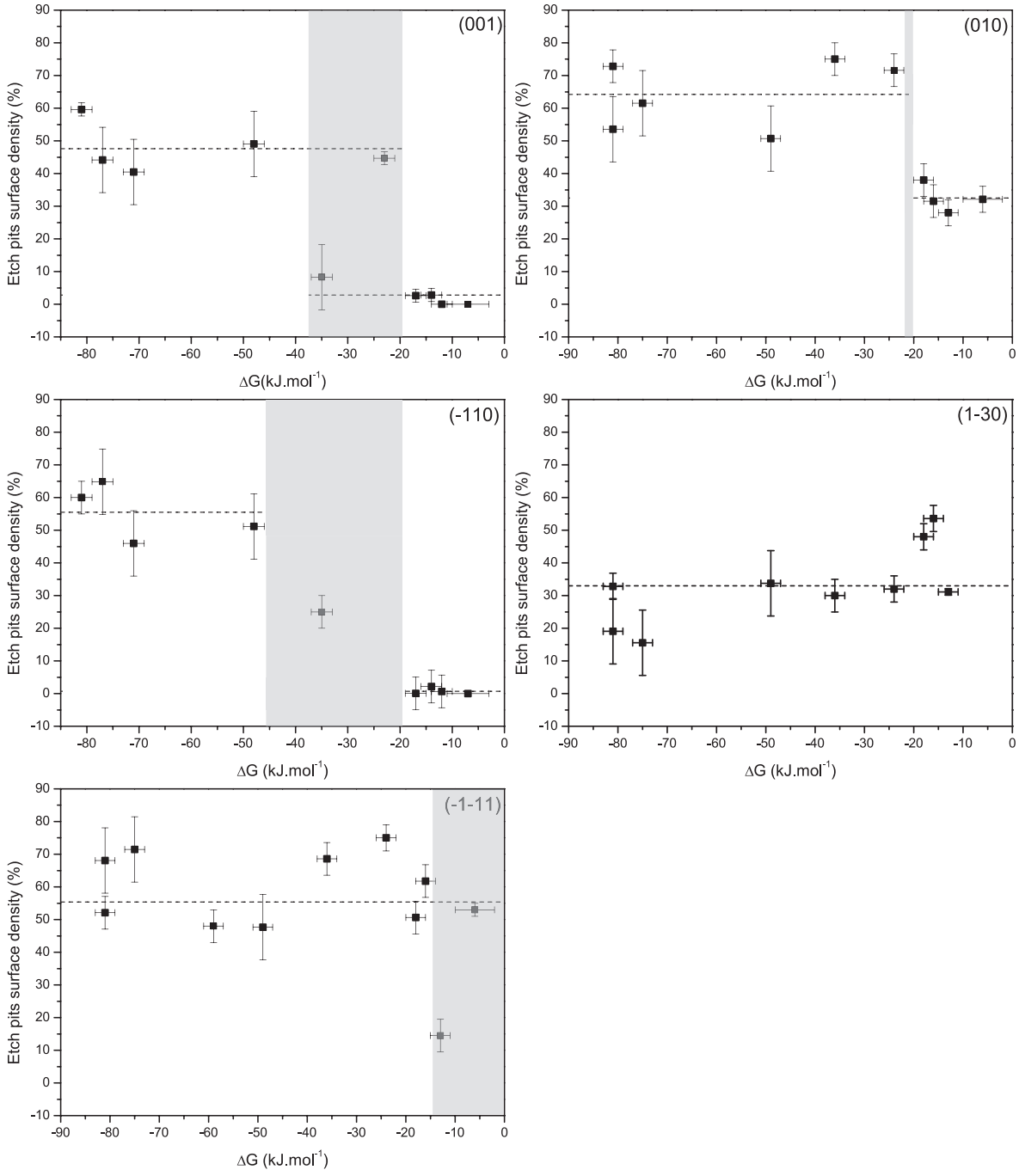

Fig. 3. Proportion of etch pits (%) covering the surface of (0 0 1), (0 1 0), ($\bar{1}$ 1 0), (1 $\bar{3}$ 0) and ($\bar{1}$ $\bar{1}$ 1) faces as a function of ΔG. A drop in the proportion of etch pits is observed for the (0 0 1), (0 1 0) and ($\bar{1}$ 1 0) faces (F1 faces) for -45 kJ mol^{-1} $\leqslant \Delta G \leqslant -20$ kJ mol^{-1} (shaded area). For the (1 $\bar{3}$ 0) and ($\bar{1}$ $\bar{1}$ 1) faces, which belong to the F2 category, no obvious modification of etch pit density can be seen for $\Delta G <\sim -10$ kJ mol^{-1}. These results illustrate that the TST framework fails to predict the r–ΔG relations and emphasizes the control exerted by the crystallographic structure on the reaction rate and rate law. In addition, these observations are consistent with the existence of a critical value of ΔG (ΔG^{crit}) as predicted by the stepwave model (Lasaga and Lüttge, 2001), where a kinetic switch is observed depending on the dominant mechanism (stepwaves originating from etch pits or dissolution at point defects and pre-existing edges and corners).

several studies (see Tullis, 1983 for a review), the occurrence of dislocations in feldspars chiefly depends on two parameters: (1) the length of the Burgers vector of the dislocation and (2) the deformation history of the minerals. From an energetic standpoint, Burgers vectors with the shortest length should be favored (i.e., for K-feldspar: [0 0 1]). In fact, dislocations oriented following the [0 0 1] direction are very common in naturally and experimentally deformed feldspars, although other Burgers vectors can also

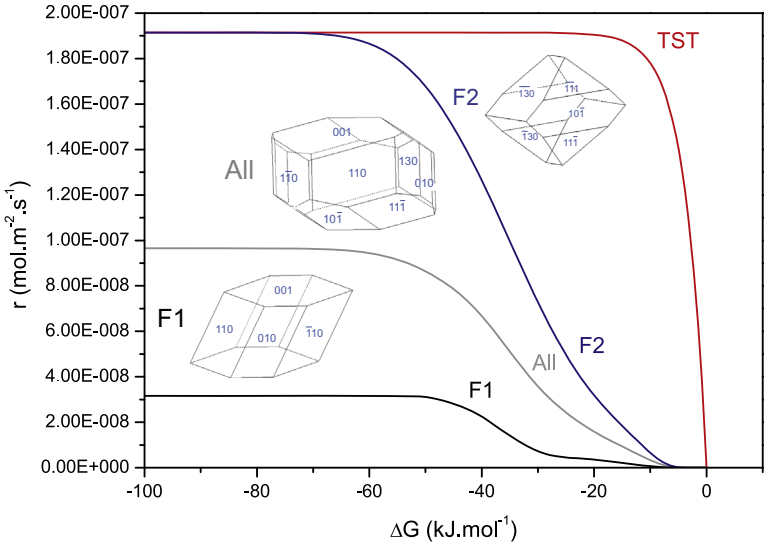

Fig. 4. Reconstruction of the r–ΔG relations for three different ideal morphologies. The curves were calculated according to the proportion of each face for three crystal habits (one composed with only F1 faces, one composed with only F2 faces, and a final one composed with all of the six faces investigated in the present study). This figure illustrates the crucial dependence of the r–ΔG relation on the expressed faces in the K-feldspar crystal morphology.

be observed, depending on the orientation of the stress applied on the crystals (Tullis, 1983). Of note, the $(1\bar{3}0)$ face is parallel to the [001] direction, such that screw dislocations with [001] Burgers vectors do not outcrop at the surface of the $(1\bar{3}0)$ face. As mentioned above, screw dislocations are often considered as important drivers for the dissolution process. Therefore, the dissolution rate of the $(1\bar{3}0)$ face may be slower than that of the other F2 faces ($(\bar{1}\bar{1}1)$ and $(\bar{1}01)$) because of the smaller number of screw dislocations outcropping at the surface of the $(1\bar{3}0)$ face. Although further work would be necessary to confirm this suggestion, it is noteworthy that the etch pit surface density is smaller for this face than for any other faces (Fig. 3), which may be considered as an indirect evidence which supports the mechanism that we propose.

4.3. On the limitations of the conventional treatment of aqueous mineral reactivity

Overall, our results demonstrate the strong anisotropic nature of aqueous mineral reactivity. The expression of such an anisotropy stems from differences in absolute face-specific dissolution rates and the non-uniqueness of $r^{(hkl)}$–ΔG relations. This anisotropic reactivity is intimately related to the anisotropic distribution of atomic crystallographic sites in the mineral structure, and its recognition has the far-reaching conceptual and methodological consequences listed below:

(i) First, defining a unique dissolution rate constant for a given mineral is intrinsically misleading, as the bulk dissolution rate of a crystal critically depends on its morphology (i.e. relative proportions of different faces exposed to the aqueous solution). Although with different arguments, the present study concurs with the conclusions reached in recent papers (e.g. Lüttge et al., 2013; Fischer et al., 2014) that using the commonplace 'bulk surface normalization approach' to provide rate constants is not appropriate to quantify the reactivity of crystalline materials that are not controlled by aqueous transport limitation or passivation. Acknowledging the anisotropic nature of aqueous mineral dissolution invalidates the use of isotropic rate laws to mechanistically account for mineral reactivity. Accordingly, deriving a single isotropic dissolution rate law for a mineral is not simply a simplification of the dissolution process, it is conceptually improper, since an overall isotropic rate law cannot capture the sensitivity of the individual faces to a given parameter.

(ii) Similarly, the conventional determination of reaction mechanisms based on measurements of bulk powder dissolution rates may be misleading. Even in the unlikely case where powders are made of grains with monodispersed morphologies, the resulting macroscopic dissolution rates remain a combination of the underlying reaction mechanisms dictated by the grain morphology: as an example, the lively debate regarding the exact shape of overall r–ΔG relations (sigmoidal or linear, see e.g. Burch et al., 1993; Oelkers et al., 1994; Gautier et al., 1994; Lasaga, 1995; Taylor et al., 2000; Hellmann and Tisserand, 2006; Beig and Lüttge, 2006; Hellmann et al., 2010) may simply vanish if one considers that the original experiments were run with powders containing different dominant morphologies (Fig. 4). Aside from offering an interpretative framework for the disparities between rate data reported in different studies as pointed out by e.g. Fischer et al., 2014, an

Table 5
Input parameters for the simulation of the evolution of crystal habit as a function of the reaction progress. The name of the crystal habit is listed in the first column. The next seven columns present the starting proportion of surface area for each face and the kinetic values $\overline{k^{(hkl)}}$ used in the model. This value corresponds to the period (i.e. the number of iterations) after which a mesh contacting the solution in a given direction dissolves. As observed experimentally, for minerals such as feldspars, some faces can dissolve ten times faster than others (e.g. $(\bar{1}\,0\,1)$ and $(\bar{1}\,\bar{1}\,1)$ faces, compared to (0 0 1), (0 1 0) and (1 1 0) faces). The dissolution period for (0 1 1) and (1 0 0) faces were arbitrarily set to 10 for simulations carried out on habit 1, 2 and 3 and to 1 for habits 1′, 2′ and 3′ (see below). The last three columns are the initial number of ECs in the crystal, the initial mesh volume and the initial crystal surface (arbitrary unit).

Habit		$(0\,0\,1)$	$(0\,1\,0)$	$(\bar{1}\,1\,0)$	$(\bar{1}\,\bar{1}\,1)$	$(\bar{1}\,0\,1)$	$(1\,0\,0)$	$(0\,1\,1)$	n_0	V_0	S_0
Habit 1 isotropic	S (%)	40.28	40.52	18.73	0.24	0.00	0.00	0.23	3.72E+08	3.72E+11	3.66E+08
	$\overline{k^{(hkl)}}$	10	10	10	10	10	10	10			
Habit 1 anisotropic	S (%)	40.28	40.52	18.73	0.24	0.00	0.00	0.23	3.72E+08	3.72E+11	3.66E+08
	$\overline{k^{(hkl)}}$	10	10	10	1	1	10	10			
Habit 2 anisotropic	S (%)	44.31	44.31	0.06	0.00	0.06	11.01	0.25	4.96E+08	4.96E+11	4.47E+08
	$\overline{k^{(hkl)}}$	10	10	10	1	1	10	10			
Habit 3 anisotropic	S (%)	19.06	44.75	8.81	0.22	26.94	0.00	0.22	5.66E+07	5.66E+10	9.67E+07
	$\overline{k^{(hkl)}}$	10	10	10	1	1	10	10			
Habit 1′ isotropic	S (%)	39.85	39.85	0.11	0.00	0.11	19.85	0.23	2.48E+08	2.48E+11	2.48E+08
	$\overline{k^{(hkl)}}$	10	10	10	10	10	10	10			
Habit 1′ anisotropic	S (%)	39.85	39.85	0.11	0.00	0.11	19.85	0.23	2.48E+08	2.48E+11	2.48E+08
	$\overline{k^{(hkl)}}$	10	10	10	1	1	1	1			
Habit 2′ anisotropic	S (%)	25.15	50.76	23.77	0.07	0.00	0.00	0.31	9.26E+07	9.26E+10	1.46E+08
	$\overline{k^{(hkl)}}$	10	10	10	1	1	1	1			
Habit 3′ anisotropic	S (%)	29.23	29.17	0.00	0.10	41.23	0.00	0.18	1.24E+08	1.24E+11	1.69E+08
	$\overline{k^{(hkl)}}$	10	10	10	1	1	1	1			

important conclusion of this work is that when dealing with powders, the impact of a macroscopic parameter as fundamental as ΔG will not lead to a unique dissolution rate, which greatly complicates the prediction of crystalline materials reactivity, even under well-defined environmental conditions.

(iii) As a final important comment, one can expect that the anisotropic aqueous mineral reactivity of crystalline materials may lead to a continuous modification of the dissolution rate of a single crystal as a function of the reaction progress, because of the gradual development of fast dissolving faces at the expense of the slower ones. This assertion was verified by monitoring numerically the dissolution features of single crystals with various morphologies. In brief, the numerical model is based on the description of a crystal by $N_x \times N_y \times N_z$ elementary cells (ECs) where N_x (respectively N_y and N_z) represents the number of ECs following x (respectively y and z) directions. The ECs have a hexahedral shape. For each EC, the model lists the number and the orientation of faces which contact the fluid. With these data, each EC is listed as belonging to a face orientation at the macroscopic scale. The ECs which have only one face in contact with the fluid belong to the macroscopic (1 0 0), (0 1 0) or (0 0 1) face (e.g. an EC which has only one face belonging to the (xOy) plane in contact with the fluid belongs to the (0 0 1) surface). In contrast, the ECs which have two non-parallel faces exposed to the solution are either assigned as (1 1 0), or (1 0 1) or (0 1 1), depending on the faces of the ECs which are exposed to the solution (e.g. the ECs whose faces exposed to the fluid are parallel to the (yOz) and (xOz) are assigned as (1 1 0). The (1 1 1) face is composed by ECs which have the three faces parallel to (xOy), (xOz), and (yOz) in contact with the fluid. For each face category, a linear retreat with time was defined, consistent with the experimental results. A constant "period" $\overline{k^{(hkl)}}$ is defined by the number of iterations required to dissolve an EC which contacts the fluid. The values of $\overline{k^{(hkl)}}$ used in simulations are listed in Table 5. As observed experimentally, some faces such as the $(\bar{1}\,0\,1)$ and $(\bar{1}\,\bar{1}\,1)$ faces dissolve ten times faster than others (e.g. (0 0 1), (0 1 0), $(\bar{1}\,1\,0)$). For the (1 0 0) or (0 1 1) faces which may enter in simulations but which were not experimentally measured, we chose an arbitrary value of 10 (Fig. 5a). Importantly, we made sure that choosing other arbitrary values for such faces do not modify the main trends which are reported below – see another set of simulations with $\overline{k^{(100)}} = \overline{k^{(011)}} = 1$ in Fig. 5b. At each time step, the model counts the number of existing ECs, the number of faces in contact with the fluid and the face orientation. These data are subsequently used to calculate the dissolved volume, the mineral surface area and, in turn, the dissolution rate per unit of area and per iteration. Simulation results for different crystal habits are presented in Fig. 5.

In spite of its simplicity (in particular, the orientation of the faces which are developed as a function of time is limited to the existing faces defined at the beginning of the simulation, and the stabilization of faces with new orientations is precluded), the first-order results show that dissolution

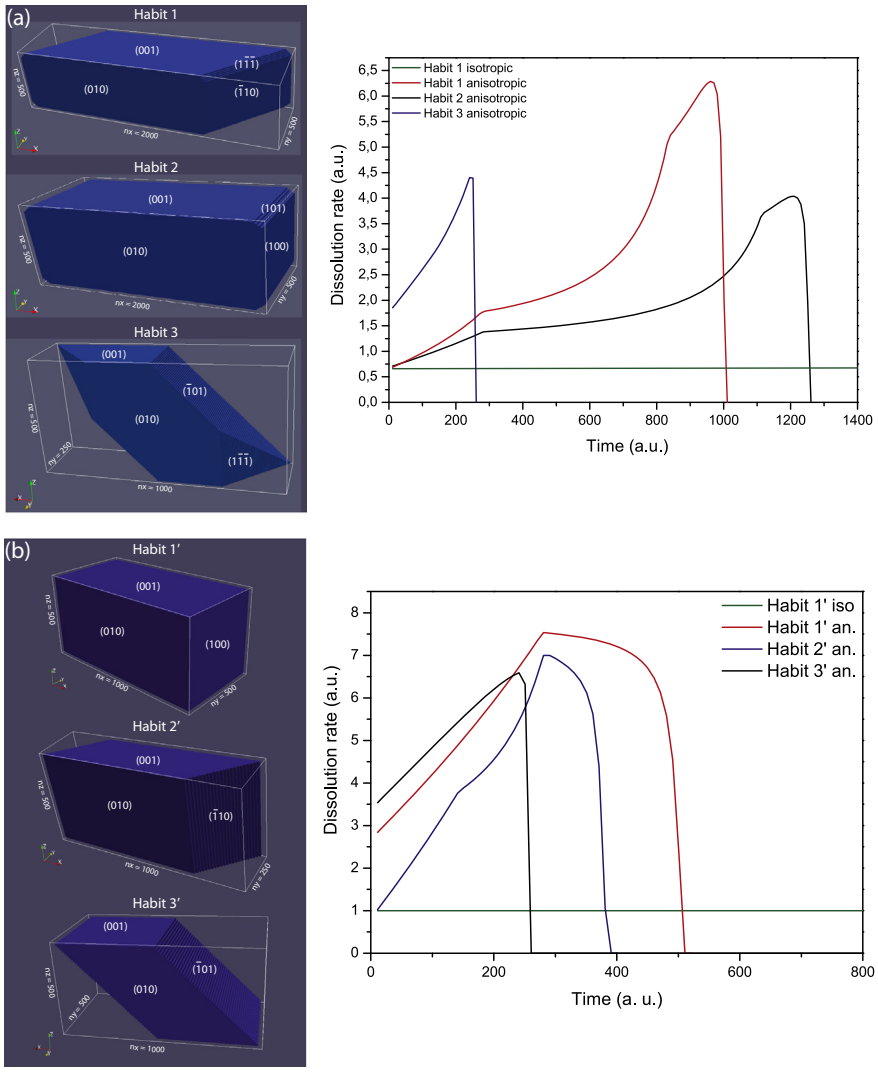

Fig. 5. Numerical results of the evolution of the dissolution rate of various arbitrary crystal morphologies over time. This figure shows the complex evolution of a crystal dissolution rate over time because of the modification of its morphology with the reaction progress. Importantly, the starting dissolution rate and its evolution depend on the initial crystal form. For the anisotropic scenarios and consistent with our experimental results for minerals such as K-feldspars, a tenfold factor between the dissolution rate of $(\bar{1}01)$ and $(\bar{1}\bar{1}1)$ faces and the others was implemented. The dissolution rate of face (100) (not measured in the present studied) was arbitrarily set to that of (a) typical F1 faces and (b) typical F2 faces. Considering K and S faces or structures more anisotropic such as that of pyroxenes (see e.g. Daval et al., 2013) would result in even more dramatic discrepancies between the various morphologies. Details of simulation parameters are listed in Table 5 and corresponding movies are available online.

anisotropy induces a complex evolution of the overall crystal dissolution rate as a function of the reaction progress. Both the onset of the overall dissolution rate and its evolution as a function of the reaction progress are primarily inherited from the starting morphology of the dissolving grains, precluding the attainment of a unique crystal habit. Similar conclusions were previously reached in the kinetic modeling study conducted by Zhang and Lüttge (2009) on albite feldspar. Regarding K-feldspar, we anticipate that such trends would be even more dramatic if K- or S-faces were implemented in the model, since their dissolution rate is expected to greatly exceed that of F2-faces. More generally, the difference between the isotropic and anisotropic scenarios can drastically increase if the rate factor between rapid and slow faces is even greater. This scenario may be encountered for very anisotropic structures such as inosilicates or phyllosilicates, where the dissolution rate of the fastest faces can be up to two orders of magnitude greater than that of the slowest faces (e.g. Daval et al., 2013), strengthening the crucial attention which should be paid to the anisotropic reactivity of dissolving minerals.

5. CONCLUSIONS

Overall, this combined experimental and modeling study illustrates some limitations of the conventional treatment of aqueous mineral reactivity. In particular, our results suggest that the mechanistic basis for the bottom-up

simulations of chemical weathering that rely on overall kinetic rate laws may not be as robust as commonly expected. Although the current reactive transport simulations cannot be simply abandoned, one has to keep in mind that most of the so-called kinetic rate laws that can be retrieved in thorough database and review papers may probably not reflect more than empirical relations, such that one has to remain careful with respect to the predictive ability of the outputs of such simulations.

Alternative approaches are therefore necessary to improve the reliability of such simulations. Although based on a simple parameterization, the model described above is unlikely to be easily implemented into reactive transport codes "as is". In fact, the variations of porosity, pore connectivity and resulting medium diffusivity as a function of the reaction progress already represents a challenge in itself (Emmanuel et al., 2015; Noiriel, 2015; Steefel et al., 2015), such that tracking the mineral and porosity textures of a mineralogical assemblage over time adds a supplementary layer of complexity which challenges its subsequent implementation in reactive transport codes. Alternatively, it may be tempting to establish detailed texture evolutions and dissolution rate laws for a limited number of equilibrium crystal habits predicted by the PBC theory, and to use the numerically-derived textures and overall dissolution rates in the corresponding simulations of porous medium weathering. However this treatment would probably be hopeless as well, because euhedral crystals are only occasionally found in the field (Velbel, 2009), where grain morphology results from the complex coupling between physical erosion and chemical weathering. Indeed, statistical investigations of the intricate interplay between mechanical breakage of crystal structures and chemical hydrolysis may represent a necessary step to isolate the dominant reaction modes and continue promoting a bottom-up treatment of mineral reactivity, for which Kinetic Monte Carlo (KMC) simulations may represent the most promising strategy (see Lüttge et al., 2013; Kurganskaya and Lüttge, 2013). Of note, as opposed to the recent successful KMC attempts on nuclear glass corrosion (see e.g. Cailleteau et al., 2008), where the simulations essentially remained underconstrained because of the large number of bond-breaking probabilities to be adjusted, multiple measurements of mineral face-specific dissolution rates can be used to over-constrain the bond-breaking probabilities implemented in KMC models for a given mineral structure. In that respect, instead of being a detrimental complicating factor, the recognition of the anisotropy of crystalline materials reactivity offers an invaluable opportunity to refine our understanding of fluid–solid reactions at a molecular-scale, paving the way for a paradigm shift in experimental measurements of aqueous mineral reactivity.

ACKNOWLEDGEMENTS

This work has been funded through a grant attributed to D.D. for the project "*Feldspar reactivity in the context of Soultz-sous-Forêts: From microstructural characterizations to numerical modeling*" under the framework of the LABEX ANR-11-LABX-0050_G-EAU-THERMIE-PROFONDE which benefits from a funding from the state managed by the French National Research Agency as part of the French "Investissements d'avenir". M.P.-V. thanks the Région Alsace and LABEX "G-EAU-THERMIE PROFONDE" for funding her PhD contract. K.G.K. effort at LBL was supported by the Director, Office of Science, Office of Basic Energy Sciences, Chemical Sciences, Geosciences, and Biosciences Division, of the U.S. Department of Energy under Contract No. DE-AC02-05CH11231.

We are indebted to G. Schäfer (Strasbourg, France) for ensuring the smooth progress of the work at LHyGeS. Thanks are due to R. Boutin, G. Morvan and A. Aubert for their help with analyses and technical contributions at the LHyGeS (Strasbourg, France). We also thank G. A. Waychunas (LBNL Berkeley, USA) for providing us the K-spar crystal used to carry out this study and R. Hellmann (ISTerre, Grenoble, France) for providing additional equipment. The insightful review of (AE) Carl Steefel and constructive and supportive comments by three anonymous reviewers were much appreciated and helped improving an earlier version of the manuscript.

APPENDIX A. SUPPLEMENTARY DATA

Supplementary data associated with this article can be found, in the online version, at http://dx.doi.org/10.1016/j.gca.2016.07.007.

REFERENCES

Aagaard P. and Helgeson H. C. (1982) Thermodynamic and kinetic constraints on reaction-rates among minerals and aqueous-solutions. 1. Theoretical considerations. *Am. J. Sci.* **282**, 237–285.

Abramoff M. D., Magalhaes P. J. and Ram S. J. (2004) Image processing with ImageJ. *Biophoton. Int.* **11**(7), 36–42.

Arvidson R. S. and Lüttge A. (2010) Mineral dissolution kinetics as a function of distance from equilibrium – new experimental results. *Chem. Geol.* **269**, 79–88.

Arvidson R. S., Beig M. S. and Lüttge A. (2004) Single-crystal plagioclase feldspar dissolution rates measured by vertical scanning interferometry. *Am. Mineral* **89**, 51–56.

Bandstra J. Z. and Brantley S. L. (2008) Surface evolution of dissolving minerals investigated with a kinetic Ising model. *Geochim. Cosmochim. Acta* **72**, 2587–2600.

Beaulieu E., Godderis Y., Donnadieu Y., Labat D. and Roelandt C. (2012) High sensitivity of the continental-weathering carbon dioxide sink to future climate change. *Nat. Clim. Change* **2**, 346–349.

Beig M. S. and Lüttge A. (2006) Albite dissolution kinetics as a function of distance from equilibrium: implications for natural feldspar weathering. *Geochim. Cosmochim. Acta* **70**, 1402–1420.

Berner R. A. (1990) Atmospheric carbon dioxide levels over phanerozoic time. *Science* **249**, 1382–1386.

Burch T. E., Nagy K. L. and Lasaga A. C. (1993) Free energydependence of albite dissolution kinetics at 80 °C and pH 8.8. *Chem. Geol.* **105**, 137–162.

Cailleteau C., Angeli F., Devreux F., Gin S., Jestin J., Jollivet P. and Spalla O. (2008) Insight into silicate-glass corrosion mechanisms. *Nat. Mater.* **7**, 978–983.

Daval D., Hellmann R., Corvisier J., Tisserand D., Martinez I. and Guyot F. (2010) Dissolution kinetics of diopside as a function of solution saturation state: Macroscopic measurements and implications for modeling of geological storage of CO2. *Geochim. Cosmochim. Acta* **74**, 2615–2633.

Daval D., Sissmann O., Menguy N., Saldi G. D., Guyot F., Martinez I., Corvisier J., Garcia B., Machouk I., Knauss K. G.

and Hellmann R. (2011) Influence of amorphous silica layer formation on the dissolution rate of olivine at 90°C and elevated pCO_2. *Chem. Geol.* **284**, 193–209.

Daval D., Hellmann R., Saldi G. D., Wirth R. and Knauss K. G. (2013) Linking nm-scale measurements of the anisotropy of silicate surface reactivity to macroscopic dissolution rate laws: new insights based on diopside. *Geochim. Cosmochim. Acta* **107**, 121–134.

Derry L. A., Kurtz A. C., Ziegler K. and Chadwick O. A. (2005) Biological control of terrestrial silica cycling and export fluxes to watersheds. *Nature* **433**, 728–731.

Emmanuel S., Anovitz L. M. and Day-Stirrat R. J. (2015) Effects of coupled chemo-mechanical process on the evolution of pore-size distributions in geological media. *Rev. Mineral. Geochem.* **80**, 45–60.

Fenter P., Zapol P., He H. and Sturchio N. C. (2014) On the variation of dissolution rates at the orthoclase (001) surface with pH and temperature. *Geochim. Cosmochim. Acta* **141**, 598–611.

Fischer C., Kurganskaya I., Schäfer T. and Lüttge A. (2014) Variability of crystal surface reactivity: what do we know? *Appl. Geochem.* **43**, 132–157.

Fritz B., Jacquot E., Jacquemont B., Baldeyrou-Bailly A., Rosener M. and Vidal O. (2010) Geochemical modelling of fluid-rock interactions in the context of the Soultz-sous-Forets geothermal system. *Cr. Geosci.* **342**, 653–667.

Gautier J. M., Oelkers E. H. and Schott J. (1994) Experimentable study of K-feldspar dissolution rates as a function of chemical affinity at 150 °C and pH 9. *Geochim. Cosmochim. Acta* **58**, 4549–4560.

Godinho J. R. A., Piazolo S. and Evins L. Z. (2012) Effect of surface orientation on dissolution rates and topography of CaF_2. *Geochim. Cosmochim. Acta* **86**, 392–403.

Godinho J. R. A., Piazolo S. and Balic-Zunic T. (2014) Importance of surface structure on dissolution of fluorite: Implications for surface dynamics and dissolution rates. *Geochim. Cosmochim. Acta* **126**, 398–410.

Golubev S. V. and Pokrovsky O. S. (2006) Experimental study of the effect of organic ligands on diopside dissolution kinetics. *Chem. Geol.* **235**, 377–389.

Gratz A. J., Manne S. and Hansma P. K. (1991) Atomic force microscopy of atomic-scale ledges and etch pits formed during dissolution of quartz. *Science* **251**, 1343–1346.

Gruber C., Zhu C., Bastian Georg R., Zakon Y. and Ganor J. (2014) Resolving the gap between laboratory and field rates of feldspar weathering. *Geochim. Cosmochim. Acta* **147**, 90–106.

Hartman P. and Perdok W. G. (1955) On the relations between structure and morphology of crystals. I. *Acta Crystallogr.* **8**, 49–52.

Hellmann R. and Tisserand D. (2006) Dissolution kinetics as a function of the Gibbs free energy of reaction: an experimental study based on albite feldspar. *Geochim. Cosmochim. Acta* **70**, 364–383.

Hellmann R., Dran J. C. and DellaMea G. (1997) The albite–water system. 3. Characterization of leached and hydrogen-enriched layers formed at 300 °C using MeV ion beam techniques. *Geochim. Cosmochim. Acta* **61**, 1575–1594.

Hellmann R., Daval D. and Tisserand D. (2010) The dependence of albite feldspar dissolution kinetics on fluid saturation state at acid and basic pH: progress towards a universal relation. *Cr. Geosci.* **342**, 676–684.

Hellmann R., Cotte S., Cadel E., Malladi S., Karlsson L. S., Lozano-Perez S., Cabié M. and Seyeux A. (2015) Nanometre-scale evidence for interfacial dissolution–reprecipitation control of silicate glass corrosion. *Nat. Mater.* **14**, 307–311.

Kampman N., Bickle M., Becker J., Assayag N. and Chapman H. (2009) Feldspar dissolution kinetics and Gibbs free energy dependence in a CO_2-enriched groundwater system, Green River, Utah. *Earth Planet Sci. Lett.* **284**, 473–488.

King H. E., Satoh H., Tsukamoto K. and Putnis A. (2014) Surface-specific measurements of olivine dissolution by phase-shift interferometry. *Am. Mineral.* **99**, 377–386.

Knauss K. G., Johnson J. W. and Steefel C. I. (2005) Evaluation of the impact of CO_2, co-contaminant gas, aqueous fluid and reservoir rock interactions on the geologic sequestration of CO_2. *Chem. Geol.* **217**, 339–350.

Kubicki J. D., Sofo J. O., Skelton A. A. and Bandura A. V. (2012) A new hypothesis for the dissolution mechanism of silicates. *J. Phys. Chem. C* **116**, 17479–17491.

Kurganskaya I. and Lüttge A. (2013) A comprehensive stochastic model of phyllosilicate dissolution: structure and kinematics of etch pits formed on muscovite basal face. *Geochim. Cosmochim. Acta* **120**, 545–560.

Laanait N., Callagon E. B. R., Zhang Z., Sturchio N. C., Lee S. S. and Fenter P. (2015) X-ray-driven reaction front dynamics at calcite–water interfaces. *Science* **349**, 1330–1334.

Lasaga A. C. (1995) Fundamental approaches in describing mineral dissolution and precipitation rates. In *Chemical Weathering Rates of Silicate Minerals* (eds. A. F. White and S. L. Brantley). Mineralogical Society of America, pp. 23–86.

Lasaga A. C. and Blum A. E. (1986) Surface chemistry, etch pits and mineral-water reactions. *Geochim. Cosmochim. Acta* **50**, 2363–2379.

Lasaga A. C. and Lüttge A. (2001) Variation of crystal dissolution rate based on a dissolution stepwave model. *Science* **291**, 2400–2404.

Lower S. K., Hochella M. F. and Beveridge T. J. (2001) Bacterial recognition of mineral surfaces: Nanoscale interactions between Shewanella and α-FeOOH. *Science* **292**, 1360–1363.

Lucca D. A., Shao L., Wetteland C. J., Misra A., Klopfstein M. J. and Nastasi M. (2006) Subsurface damage in (100) ZnSe introduced by mechanical polishing. *Nucl. Instrum. Methods Phys. Res., Sect. B* **249**, 907–910.

Lüttge A., Bolt E. W. and Lasaga A. C. (1999) An interferometric study of the dissolution kinetics of anorthite; the role of reactive surface area. *Am. J. Sci.* **299**, 652–678.

Lüttge A., Arvidson R. S. and Fischer C. (2013) A stochastic treatment of crystal dissolution kinetics. *Elements* **9**, 183–188.

Maher K. and Chamberlain C. P. (2014) Hydrologic regulation of chemical weathering and the geologic carbon cycle. *Science* **343**, 1502–1504.

Maher K., Steefel C. I., White A. F. and Stonestrom D. A. (2009) The role of reaction affinity and secondary minerals in regulating chemical weathering rates at the Santa Cruz Soil Chronosequence, California. *Geochim. Cosmochim. Acta* **73**, 2804–2831.

Maher K., Johnson N. C., Jackson A., Lammers L. N., Torchinsky A. B., Weaver K. L., Bird D. K. and Brown, Jr, G. E. (2016) A spatially resolved surface kinetic model for forsterite dissolution. *Geochim. Cosmochim. Acta* **174**, 313–334.

Nicoleau L., Nonat A. and Perrey D. (2013) The di- and tricalcium silicate dissolutions. *Cem. Concr. Res.* **47**, 14–30.

Noiriel C. (2015) Resolving time-dependent evolution of pore-scale structure, permeability and reactivity using X-ray microtomography. *Rev. Mineral. Geochem.* **80**, 247–285.

Oelkers E. H., Schott J. and Devidal J.-L. (1994) The effect of aluminum, pH, and chemical affinity on the rates of aluminosilicate dissolution reactions. *Geochim. Cosmochim. Acta* **58**, 2011–2024.

Ohlin C. A., Villa E. M., Rustad J. R. and Casey W. H. (2010) Dissolution of insulating oxide materials at the molecular scale. *Nat. Mater.* **9**, 11–19.

Palandri, J. L. and Kharaka, Y. K. (2004) A compilation of rate parameters of water–mineral interaction kinetics for application to geochemical modeling, in: *U.S. Geological Survey* (ed. O.F. R.), p. 70.

Ruiz-Agudo E., Putnis C. V., Rodriguez-Navarro C. and Putnis A. (2012) Mechanism of leached layer formation during chemical weathering of silicate minerals. *Geology* **40**, 947–950.

Saldi G. D., Daval D., Guo H., Guyot F., Bernard S., Le Guillou C., Davis J. A. and Knauss K. G. (2015) Mineralogical evolution of Fe–Si-rich layers at the olivine-water interface during carbonation reactions. *Am. Mineral.* **100**, 2655–2669.

Saldi G. D., Daval D., Morvan G. and Knauss K. G. (2013) The role of Fe and redox conditions in olivine carbonation rates: An experimental study of the rate limiting reactions at 90 and 150 °C in open and closed systems. *Geochim. Cosmochim. Acta* **118**, 157–183.

Schneider C. A., Rasband W. S. and Eliceiri K. W. (2012) NIH Image to ImageJ: 25 years of image analysis. *Nat. Methods* **9**, 671–675.

Schott J., Pokrovsky O. S. and Oelkers E. H. (2009) The link between mineral dissolution/precipitation kinetics and solution chemistry. *Rev. Mineral. Geochem.* **70**, 207–258.

Smith M. E., Knauss K. G. and Higgins S. R. (2013) Effects of crystal orientation on the dissolution of calcite by chemical and microscopic analysis. *Chem. Geol.* **360–361**, 10–21.

Steefel C. I., Beckingham L. E. and Landrot G. (2015) Micro-continuum approaches for modeling pore-scale geochemical processes. *Rev. Mineral. Geochem.* **80**, 217–246.

Taylor A. S., Blum J. D. and Lasaga A. C. (2000) The dependence of labradorite dissolution and Sr isotope release rates on solution saturation state. *Geochim. Cosmochim. Acta* **64**, 2389–2400.

Tullis, J. (1983) Deformation of feldspars. In: *Feldspar Mineralogy. Reviews in Mineralogy* (ed. P.H. Ribbe), **2**, 297–323.

Turpault M. P. and Trotignon L. (1994) The dissolution of biotite single-crystals in dilute HNO_3 at 24 °C – evidence of an anisotropic corrosion process of micas in acidic solutions. *Geochim. Cosmochim. Acta* **58**, 2761–2775.

van der Lee, J. and De Windt, L. (2002) CHESS Tutorial and Cookbook. Updated for version 3.0., Paris.

Velbel M. A. (2009) Dissolution of olivine during natural weathering. *Geochim. Cosmochim. Acta* **73**, 6098–6113.

White A. F. and Brantley S. L. (2003) The effect of time on the weathering of silicate minerals: why do weathering rates differ in the laboratory and field? *Chem. Geol.* **202**, 479–506.

Woensdregt C. F. (1982) Crystal morphology of monoclinic potassium feldspar: a qualitative approach with special emphasis on the Periodic Bond Chain Theory of Hartman and Perdrok. *Z. Kristallogr.* **161**, 15–33.

Yanina S. V. and Rosso K. M. (2008) Linked reactivity at mineral–water interfaces through bulk crystal conduction. *Science* **320**, 218–222.

Zhang L. and Lüttge A. (2009) Morphological evolution of dissolving feldspar particles with anisotropic surface kinetics and implications for dissolution rate normalization and grain size dependence: a kinetic modeling study. *Geochim. Cosmochim. Acta* **73**, 6757–6770.

Associate editor: Carl Steefel